IEEE Access
Multidisciplinary | Rapid Review | Open Access Journal

Received August 20, 2019, accepted August 30, 2019, date of publication September 12, 2019,
date of current version September 25, 2019.

Digital Object Identifier 10.1109/ACCESS.2019.2940766

Ultrasonic Computerized Tomography Imaging Method With Combinatorial Optimization Algorithm for Concrete Pile Foundation

GUAN WANG[1,2], YAO CHEN[2], QIUFENG LI[1,2], CHAO LU[2], GUO CHEN[2], AND LIXIA HUANG[2]

[1]Key Laboratory of Jiangxi Province for image processing and pattern recognition, Nanchang Hangkong University, Nanchang 330063, China
[2]Key Laboratory of Nondestructive Testing (Ministry of Education), Nanchang Hangkong University, Nanchang 330063, China

Corresponding authors: Qiufeng Li (qiufenglee@nchu.edu.cn) and Chao Lu (luchao@nchu.edu.cn)

This work was supported in part by the National Natural Science Foundation of China under Grant 11764030, in part by the Special Plan for the Construction of Superiority Scientific and Technological Innovation Teams in Jiangxi Province under Grant 20171BCB24008, in part by the Open Foundation of Key Laboratory of Jiangxi Province for Image Processing and Pattern Recognition under Grant ET201804043, and in part by the Science and Technology Project of Jiangxi Education Department under Grant GJJ170577.

ABSTRACT Concrete pile foundations are the main load-carrying and aseismic structures for many large-scale building structures. Their structural quality will have a great impact on the safety of building structures. However, the imaging results still cannot easily meet practical demands in current ultrasonic Computerized Tomography (CT) imaging tests of concrete structures. In view of the current difficulties, a combinatorial optimization tomographic imaging method is proposed. First, a quadric broadening objective function with a clear physical meaning is established according to the characteristics of ultrasonic propagation in concrete. Then, a new CT imaging method of concrete pile foundation is formed by combining fast adaptive optimization search ability of Genetic Algorithm (GA) with the global search control ability of Simulated Annealing Algorithm (SAA). The numerical simulation experiments have shown that the usage of the correct priori information and the excellent characteristic of the Simulated Annealing Genetic Algorithm (SAGA) in searching for the global minimum value of the function have produced accurate and effective results with stable numerical values. Finally, the imaging method is verified by experiment, where results show that SAGA requires fewer iterations, has faster computation speed and gives more accurate imaging results compared with the single GA.

INDEX TERMS Concrete pile foundation, ultrasonic CT, inversion imaging algorithm, combinatorial optimization algorithm, SAGA.

I. INTRODUCTION

As one of the most important building materials at present, concrete is not only cheap and easy to produce but also has strong compression resistance, long life and high hardness. Therefore, the use of concrete is increasing rapidly in civil engineering. Given its importance in the load capacity and seismic resilience of buildings, the structural quality of concrete pile foundations have a tremendous impact on the safety of building structures [1], [2]. However, whether in-service or newly completed, there are often concrete pile foundation defects such as voids, inclusions and uneven strength in the structure because of design or construction flaws, which pose a difficult challenge for modern testing technologies [3]–[5].

The associate editor coordinating the review of this manuscript and approving it for publication was Huimin Lu.

Of the five traditional non-destructive testing (NDT) methods, radiographic testing uses high-frequency and high-energy particles to penetrate the concrete and determine internal conditions. However, these high-energy particles attenuate strongly in concrete, so radiographic testing is not suitable for this purpose. Magnetic particle testing, eddy current testing and penetration testing are also not suitable because of their testing characteristics. Therefore, ultrasonic testing has become the most common method for NDT of concrete [6]–[8].

At present, according to the purpose of detection, the common testing methods for pile mainly include: static load method, core drilling method, reflected wave method and acoustic wave transmission method. The purpose of the static load method is to solve the vertical compressive bearing capacity of the pile, and analyze and calculate the late

This work is licensed under a Creative Commons Attribution 4.0 License. For more information, see http://creativecommons.org/licenses/by/4.0/

TABLE 1. Comparison of existing pile test methods.

METHODS	DESTRUCTIVENESS	OBJECTIVE	LOCATION	LOCATION ACCURACY	VISUALIZATION
Static load method	NO	Evaluation of bearing capacity	NO	/	NO
Core drilling method	YES	Evaluation of quality and strength	PART	MIDDLE	NO
Reflected wave method	NO	Evaluation of integrity	NO	LOW	NO
Half-amplitude method	NO	Detection of damage	PART	MIDDLE	NO
Inclined survey method	NO	Detection of damage	YES	MIDDLE	NO
CT imaging method	**NO**	**Detection of damage**	**YES**	**HIGH**	**YES**

settlement of the building according to the settlement of the pile top in the vertical compression and static load test of the single pile. The core drilling method is a micro-breakage detection method. It can detect the quality and strength of the concrete pile through detecting the core. The reflected wave method is to load low-energy signals at the top of the pile. The signal excitation mode is divided into steady-state excitation and transient excitation. The speed-admittance curves are used to evaluate the integrity of the pile [9], [10]. All of the above methods evaluate the pile by local sampling and signal characteristics, which have certain limitations.

However, the acoustic wave transmission method is a method for judging the type of the pile defect and position by detecting the changes of the acoustic parameters. The method has been widely used in the detection of concrete piles foundations.

Traditional acoustic wave transmission methods for concrete pile foundations use the half-amplitude and the inclined survey methods. They also combine probabilistic and empirical methods to extract meaningful information. However, these testing methods can only give qualitative or semi-quantitative testing conclusions, depending on the experience of testing personnel and being unable to provide accurate defect quantification [11]–[13]. In recent years, the combination of tomography and ultrasonic detection has achieved good detection results and been widely used [14], [15]. Usually, the sound velocity of each unit can be obtained one by one through forward calculation of acoustic propagation path and inversion imaging. And then reliable profile images can be provided after image superposition and smoothing [16]–[19]. The characteristics of these methods are shown in Table 1.

At present, acoustic propagation path tracing algorithms are relatively mature, and high precision forward calculation results can be obtained [20]–[22]. The key to tomographic imaging results is the tomographic inversion algorithm, which is also a hotspot of current research. The classical iterative inversion algorithms, ART and SIRT, are local continuous optimizations. For multi-extremum inversion functions, only local solutions can be obtained, which often results in inaccuracies. On this basis, some improved inversion methods have achieved better results in some aspects, but still fail to meet the practical requirements in terms of inversion calculation speed, stability and accuracy for concrete pile foundation [23], [24]. Modern combinatorial optimization algorithms have unique advantages. Depending on the application, their respective advantages can be obtained by combining two or more algorithms, which will be conducive to not only finding a global optimal solution and improving imaging accuracy, but also improving the speed of the algorithm.

In this paper, we combine a Simulated Annealing Algorithm (SAA) with a Genetic Algorithm (GA). The GA offers faster and higher-precision combinatorial optimization calculation, while the SAA is used to find the optimal solution in the global scope and avoid premature convergence and local optima. That is, by adding a reasonable disturbance in the early solution of GA, we avoid local solutions and approach the global optimal solution as soon as possible [25], [26].

II. PRINCIPLE OF SAGA TOMOGRAPHIC INVERSION ALGORITHM

Tomographic inversion algorithms originate from medical CT imaging technology, also known as image reconstruction

technology. The purpose is to obtain the internal profile image of the detected object based on the path data obtained by forward calculation, inversion calculation and velocity distribution diagrams [27], [28]. However, it is very difficult to calculate the solution of the large linear equations formed by forward calculation accurately because of the large amount of data, incompatibility and ill-condition of the equations. In order to facilitate the application of combinatorial optimization algorithms to solve the equations, the augmented objective function **F(x)** of quadratic optimization is constructed by using the minimum distance criterion and the prior constraint criterion of ultrasonic propagation as follows [29]:

$$\mathbf{F}(\mathrm{x}) = (\mathbf{T} - \mathbf{AX})' \bullet \mathbf{D}_1^{-1} \bullet (\mathbf{T} - \mathbf{AX}) + \mu(\mathbf{X} - \mathbf{X_0})' \bullet \mathbf{D}_2 \bullet (\mathbf{X} - \mathbf{X}_0). \quad (1)$$

where $\mathbf{X}$ is the value to be evaluated. $\mathbf{X}_0$ is the slowness vector of the prior model. $\mathbf{A}$ is projection matrix and $\mathbf{D_1}$ and $\mathbf{D_2}$ are diagonal matrices. The diagonal elements of $\mathbf{D}_2$ are the products of ultrasonic crossing unit length and its velocity, while μ is the damping parameter, which determines the relative weight between the two terms on the right side of equation (1). The objective function can be used to improve the validity of the short-distance path information and increase the weight of pixels with more ultrasonic path traversal and more information to improve the validity of the pixel information.

SAA was first proposed by Metropolis in 1953. In 1983, Kirkpatrick proposed a stochastic optimization algorithm based on the Monte Carlo iterative solution strategy, and applied SAA to it [30], [31]. At present, this algorithm has been applied in fields such as production scheduling, control engineering, machine learning, neural networks and signal processing [32], [33].

The probability expression of SAA according to the Metropolis criterion is as follows:

$$P_r = \begin{cases} 1, & EN_{new} < EN_{old} \\ \exp(\dfrac{EN_{old} - EN_{new}}{T}), & EN_{new} \geq EN_{old}. \end{cases} \quad (2)$$

where P_r is the cooling probability. T is the temperature value. EN is the internal energy at temperature T. This criterion accepts a result that is inferior to the current solution with a certain probability, which makes it possible to jump out of the local optimal solution. Thus, it allows us to avoid falling into a local solution in the search process, and leads to the global optimal solution quickly [34].

GA is an adaptive algorithm proposed by Professor Holland in 1975. It simulates the evolutionary law of the biological world and is a randomized search method. The algorithm has the characteristics of automatically adjusting the search direction without definite rules and is widely used in the fields of artificial intelligence, combinatorial optimization, machine learning and adaptive control [35], [36]. The GA is realized through the three cycles of selection, crossover and mutation, as shown in Fig. 1. The condition for cycle termination is to obtain the required population or the specified number of iterations. In Fig. 1, the cycle diagram starts with a population. After the survival of the fittest, the optimal part forms a new population and the population generates subpopulations through crossover. In the process of evolution, some individuals in the population also show mutation characteristics, and then turn into a next generation population, which becomes the beginning of a new cycle. Therefore, GA makes the global search process more efficient [37].

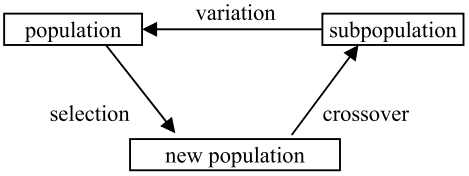

FIGURE 1. Diagram of cycle computation for genetic algorithms.

However, when GA is applied to solving large equations, problems such as local optima or premature convergence still arise, and the solving process needs to be further optimized. Therefore, we combine the characteristics of SAA and GA, and introduce SAA into GA to form a combinatorial optimization algorithm based on a Simulated Annealing Genetic Algorithm (SAGA), which can avoid the above problems effectively. The relative individual fitness p_i is calculated through equations (3) and (4):

$$p_i = \frac{e^{f_i/T}}{\sum_{i=1}^{M} e^{f_i/T}}. \quad (3)$$

$$T = T_0 \bullet (0.99^{g-1}). \quad (4)$$

where M is the population size, which is determined according to the requirements. f_i is the fitness of the ith individual, which generally takes the objective function value. T_0 is the initial temperature and g is the genetic algebra. The two variables are determined according to the calculation requirements. T is the temperature, which can be carried out through equation (4). The crossover probability P_c and mutation probability P_m can be calculated automatically according to equations (5) and (6) according to the differences of individual fitness. That is, the increase or decrease of the crossover and mutation rates is determined according to the consistency of individual fitness results. In addition, the algorithm can also improve the search accuracy.

$$P_c = \begin{cases} \dfrac{k_1(f_{\max} - f)}{f_{\max} - f_{avg}}, & f \geq f_{avg} \\ k_2, & f < f_{avg}. \end{cases} \quad (5)$$

$$P_m = \begin{cases} \dfrac{k_3(f_{\max} - f')}{f_{\max} - f_{avg}}, & f' \geq f_{avg} \\ k_4, & f' < f_{avg}. \end{cases} \quad (6)$$

In the equations (5) and (6), $f_{\max}$ refers to the maximum fitness of the population. f_{avg} is the population average fitness. f refers to the larger fitness of the crossed individuals

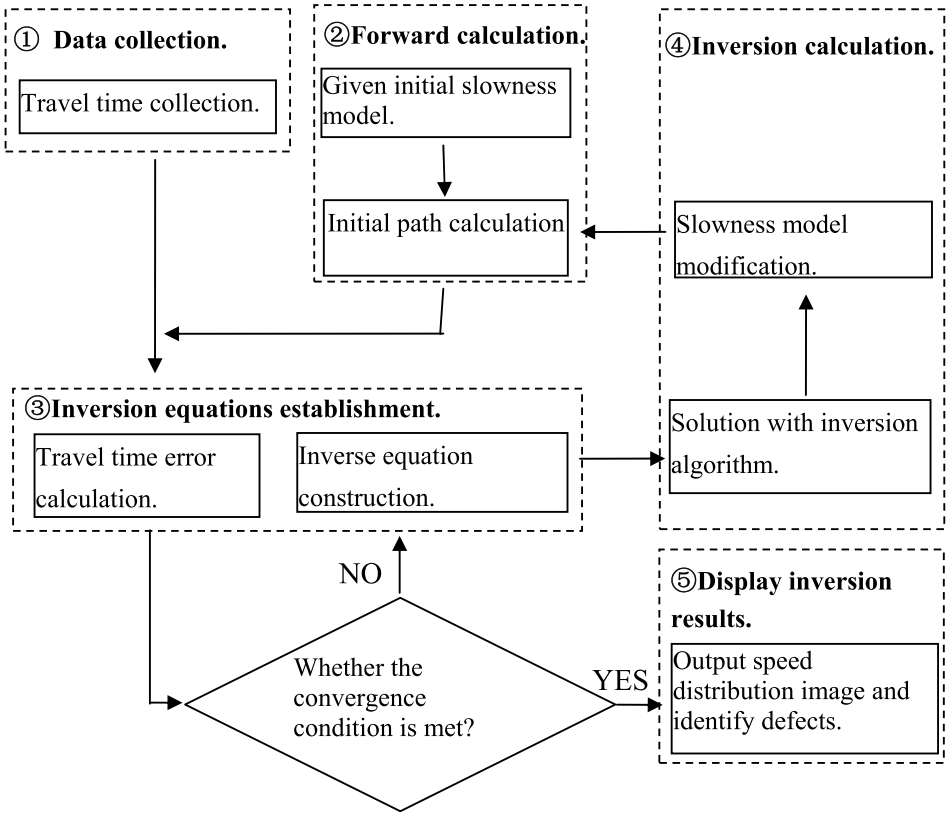

FIGURE 2. Structural diagram of CT imaging system.

of the father generation. f ' is the fitness of the individual to be mutated while k_1, k_2, k_3 and k_4 are constants. Fig.2 is the structural diagram of CT imaging system. The main steps of SAGA algorithm are as follows [38], [39]:

Step 1: Give the initial temperature of SAA T_0 and perform cooling according to equation (4). At the same time, the initial population is generated to determine the number of random individuals M and the total genetic algebra g.

Step 2: Calculate the selected fitness f_i of each individual according to equation (3).

Step 3: Determine whether the termination conditions are satisfied: (1) whether the total genetic algebra g is reached; (2) whether T has been reduced to 0. If either or both of these conditions have been met, Step 7 is executed; if neither condition is met, Step 4 is executed.

Step 4: Roulette selection is adopted to select individuals according to their selection fitness f_i. The crossover probability P_c and mutation probability P_m are calculated according to equations (5) and (6). The crossover and mutation operations are completed to generate new individuals.

Step 5: We decide whether to accept the new individual obtained in Step 4 depending on the probability of the Metropolis criterion in equation (2). If so, the corresponding father individual is replaced by the accepted new individual, thus generating a new population.

Step 6: Calculate the temperature T of the next cycle according to equation (4), and return to Step 2 for execution.

Step7: Output the optimal solution that meets the requirements.

III. NUMERICAL SIMULATION

A. MODEL ESTABLISHMENT

Simulation experiments has been performed using the finite element software ABAQUS which can analyze a complex system of solid mechanics and structural mechanics. ABAQUS is also applicable for the modeling and analysis of the process of ultrasonic wave propagation in solids. 2D model of concrete structure is established as shown in Fig.3. The whole testing area is 1000mm×980 mm. Section A in Fig.3 expresses the low-speed zone and section B is the high-speed zone. The section outside of A and B is concrete materials. The ultrasonic velocity v of each section in the model is calculated in accordance with equation (7). In the equation (7), ρ indicates material density; E indicates material modulus of elasticity; δ indicates material poisson's ratio. The velocity of each section can be calculated by using the material parameters given in Table 2. After the calculation process, the resultant ultrasonic velocity of concrete area is 3892.7 m/s, high-speed section 4165.3 m/s and low-speed

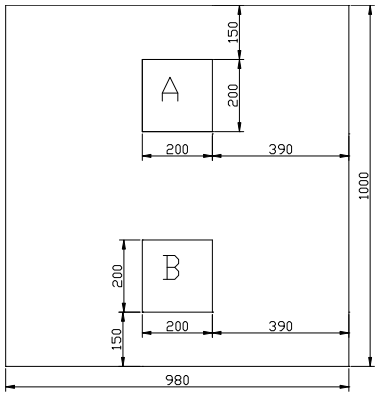

FIGURE 3. Simulation concrete model by ABAQUS (Unit: mm).

TABLE 2. Material parameters in the simulation.

Model area	ρ / kg/m^3	E / Mpa	δ
Concrete	2600	35000	0.21
high-speed section	2800	38000	0.28
Low-speed section	2200	30000	0.19

section 3869.2 m/s.

$$v = \sqrt{\frac{E}{\rho}} \cdot \sqrt{\frac{(1-\delta)}{(1+\delta)(1-2\delta)}}. \tag{7}$$

B. SIMULATION DETECTIONG AND RESULTS ANALYSIS

In order to ensure strong penetrating power and small attenuation during the propagation process of ultrasound in the concrete, testing frequency range is from 50 kHz to 500 kHz. Gaussian signal is selected as excitation signal in the ultrasonic numerical simulation for concrete structure, and the analog ultrasonic source is obtained as shown in the following equation:

$$h(t) = \sin(2\pi ft) \cdot e^{(-((t-t_p)\cdot w)^2)}. \tag{8}$$

where f is the central frequency; w is a pulse-width coefficient of Gaussian pulse; t_p is the positional parameter of the entire waveform in the transmitting cycle. Actual simulation waveform and its spectrum are shown in Fig.4, and central frequency of the signal is 50 kHz.

In the simulation detection, according to the sound velocity of 3869.2 m/s in the low speed area, the wavelength of the ultrasonic wave in the concrete is about 77.4 mm. Therefore, according to the grid size should be less than 1/10 of the wavelength, and the simulation mesh size is set to 7mm [40], [41].

The simulation detecting method is illustrated in Fig.5. The ultrasonic wave is excited from the left side of the concrete model. There are totally nine excitation positions from top to bottom labeled as T1-T9. On the right side, there are nine

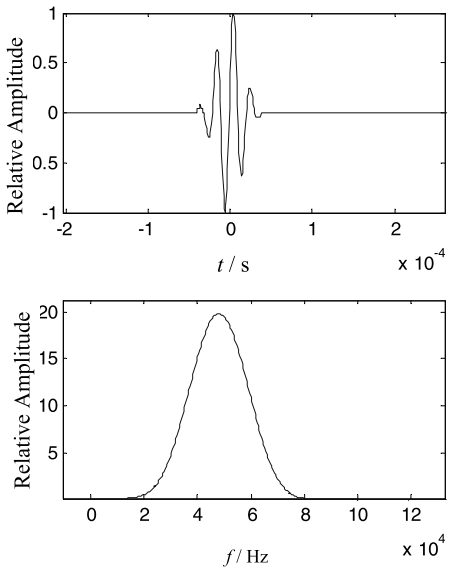

FIGURE 4. Waveform and spectrum of excitation pulse.

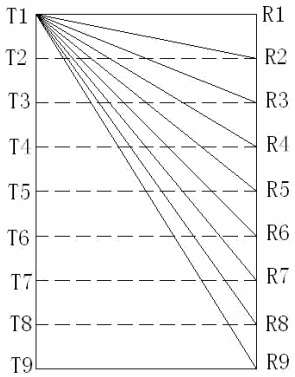

FIGURE 5. The signal exciting and receiving method diagram.

receiving positions as can be seen in the figure (R1-R9). Thus there are a total of 81 travel time data.

Firstly, the detecting model is divided into 9×9 pixel units and forward computation is carried out by using the test data in accordance with the classic curved ray tracing method resulting in the calculation of all ultrasonic propagating paths. Then GA and the SAGA inversion methods are applied respectively to calculate the ultrasonic velocity of each pixel unit. During the GA processing, the ideal controlling parameters are obtained after repetitious experiments, whereas the primary parameters are computed as follows: the population size is 60; the crossover probability is 0.92; the mutation probability is 0.05 and the genetic generation is 500. The adaptive crossover probability and mutation probability are applied in the SAGA. Furthermore the objective function provided in Equation(1) and SAA are introduced in the SAGA to improve the stability and the convergence. Finally, the CT results of ultrasonic velocity are obtained as shown in Fig.6 and Fig.7 respectively.

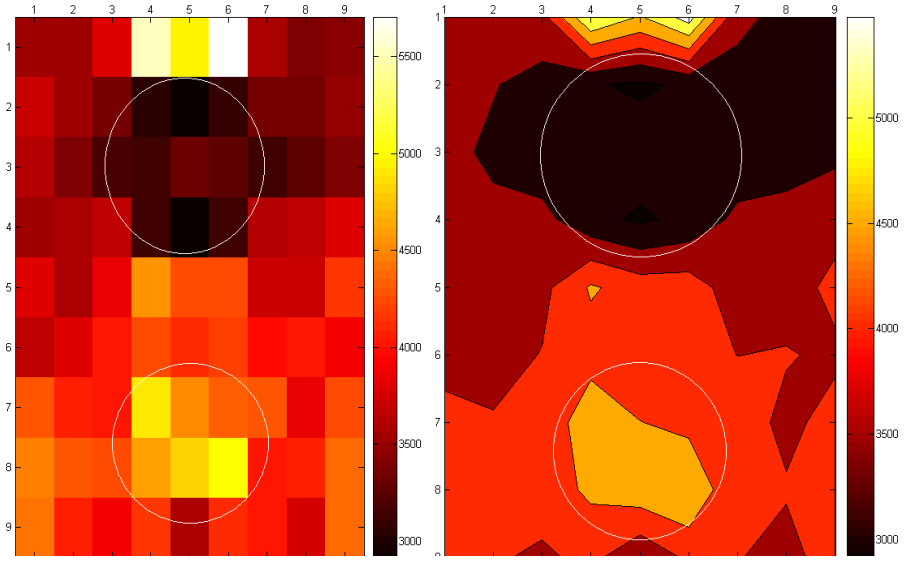

FIGURE 6. The ultrasonic CT results processed by GA. (a) Velocity chart; (b) Velocity contour map.

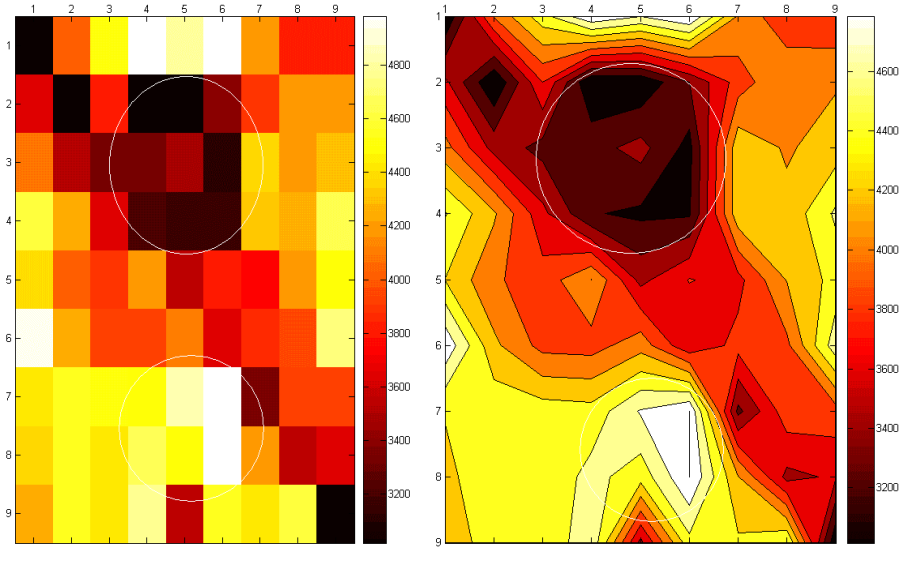

FIGURE 7. The ultrasonic CT results processed by SAGA. (a) Velocity chart; (b) Velocity contour map.

Fig.6(a) and Fig.7(a) illustrate the ultrasonic velocity map of each pixel unit corresponding to its position in the model, processed by GA and the SAGA respectively. Fig.6(b) and Fig.7(b) express velocity contour map of each pixel unit processed by both methods. These velocity contour maps are used to estimate the defected region. The defect positions can be clearly distinguished in the figures. The circled area at the top section of the contour map figures is the low-speed defect area and the area marked out at lower section is the high-speed defect area. The results of the two inversion algorithms were analyzed and compared through Table 3. It can be seen from the table that the inversion imaging results produced by the SAGA are more accurate and steady than the ones calculated by GA. The SAGA results are also closer to the real ultrasonic velocity.

IV. EXPERIMENTAL RESULTS AND ANALYSIS

A. PREPARATION OF PILE FOUNDATION SPECIMEN

The specimen design of the experimental concrete pile foundation is shown in Fig. 8(a). The size of the specimen was $1200\times300\times1000$ mm^3. In order to facilitate the placement of sensors to collect scanning data, two sound tubes with

TABLE 3. Ultrasonic velocity inversion results of the Simulation model.

Algorithm	Average speed of inversion background (m/s)	Relative error to true value (%)	Inversion defects average speed of sound (low / high speed) (m/s)	The defect section error (low / high speed) (%)
GA	3989.5	2.49	3692.2/4074.8	4.57/2.17
SAGA	**3840.3**	**1.35**	**3830.2/4196.4**	**1.01/0.75**

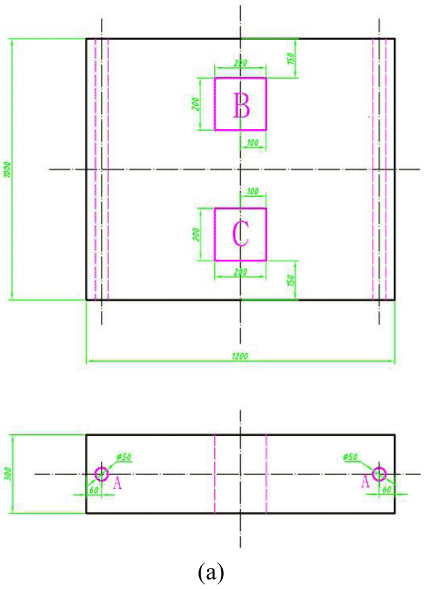

(a)

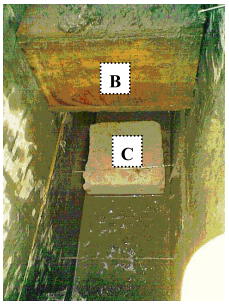

(b)

(c)

FIGURE 8. Diagram sketch of the concrete pile foundation specimen. (a) Design drawing of the specimen; (b) Internal structure of specimen before pouring; (c) Overall photo of the specimen after pouring.

a diameter of 50 mm were preset at position A. At the same time, a high-speed defect and a low-speed defect were preset in the middle part of the specimen. The sizes of the defects were both $300\times200\times200$ mm^3. The low-speed defect in position B was a cavity, while the high-speed defect in position C was a mortar block. The design strength of the specimen was C25. A model of the specimen was constructed by using wood, and then cement, medium-sized sand and aggregate was poured in accordance with the conventional concrete mixing ratio. The actual internal structure of specimen before pouring and overall photo of the specimen after pouring are shown in Fig. 8(b) and Fig. 8(c). The position of the sound tubes (A), the low-speed defect (B) and the high-speed defect (C) have been marked in the figure.

B. EXPERIMENTAL PROCESS

The ultrasonic testing instrument used for the pile foundation specimen is shown in Fig. 9. The center frequency of the testing sensor was 50 kHz. The sensor collected the time of sound travel from different measuring points in the sound tube through transmission and reception, which provided data for the imaging system. Before the experiment, the detection area of the specimen was roughly divided into a grid of size 14×14, and then water was injected into the sound tube. The transmitter and receiver sensors were placed at the measuring points of the two sound tubes according to the position displayed by the depth markers, respectively. The sector scanning mode was adopted and the scanning diagram is shown in Fig. 10. The letter T in the figure represents the transmitting sensor and letter R represents the receiving sensor.

FIGURE 9. Non-metallic ultrasonic testing instrument.

Fig. 11 shows the field test photo. The transmitting and receiving sensors were both placed at the bottom of the two sound tubes (i.e. the first test point) according to the grid preset. After receiving the data from the first test point, the receiving sensor was moved to the second test point and we again sampled. Sampling was repeated until the last test point at the top (the 14th test point), at which point the

TABLE 4. Measured data of travel time from each transmitting sensor to each receiving sensor. (unit: ms).

	R1	R2	R3	R4	R5	R6	R7	R8	R9	R10	R11	R12	R13	R14
T1	0.2776	0.2800	0.2824	0.2808	0.2788	0.2780	0.2784	0.2796	0.2812	0.2832	0.2860	0.2904	0.2960	0.3008
T2	0.2808	0.2828	0.2808	0.2780	0.2768	0.2760	0.2756	0.2764	0.2772	0.2784	0.2816	0.2860	0.2908	0.2964
T3	0.2864	0.2852	0.2816	0.2784	0.2764	0.2752	0.2740	0.2732	0.2740	0.2744	0.2780	0.2816	0.2856	0.2900
T4	0.2900	0.2852	0.2828	0.2788	0.2752	0.2720	0.2704	0.2704	0.2704	0.2708	0.2728	0.2752	0.2800	0.2828
T5	0.2908	0.2852	0.2812	0.2756	0.2716	0.2692	0.2664	0.2648	0.2652	0.2656	0.2668	0.2700	0.2744	0.2772
T6	0.2900	0.2848	0.2796	0.2744	0.2700	0.2656	0.2608	0.2624	0.2616	0.2620	0.2624	0.2664	0.2700	0.2728
T7	0.2912	0.2840	0.2804	0.2740	0.2692	0.2652	0.2640	0.2632	0.2628	0.2616	0.2632	0.2632	0.2672	0.2700
T8	0.2928	0.2884	0.2828	0.2760	0.2708	0.2672	0.2652	0.2628	0.2620	0.2616	0.2600	0.2628	0.2652	0.2664
T9	0.2968	0.2916	0.2844	0.2784	0.2736	0.2688	0.2648	0.2628	0.2632	0.2604	0.2604	0.2616	0.2640	0.2664
T10	0.3012	0.2936	0.2876	0.2808	0.2760	0.2684	0.2664	0.2656	0.2628	0.2588	0.2612	0.2624	0.2640	0.2668
T11	0.3072	0.2988	0.2924	0.2848	0.2788	0.2740	0.2712	0.2668	0.2656	0.2632	0.2636	0.2648	0.2668	0.2688
T12	0.3132	0.3056	0.2972	0.2880	0.2848	0.2784	0.2732	0.2728	0.2688	0.2676	0.2664	0.2684	0.2696	0.2720
T13	0.3188	0.3084	0.3028	0.2948	0.2888	0.2836	0.2788	0.2768	0.2732	0.2716	0.2704	0.2708	0.2732	0.2712
T14	0.3264	0.3168	0.3084	0.3012	0.2932	0.2872	0.2852	0.2820	0.2796	0.2784	0.2756	0.2764	0.2764	0.2728

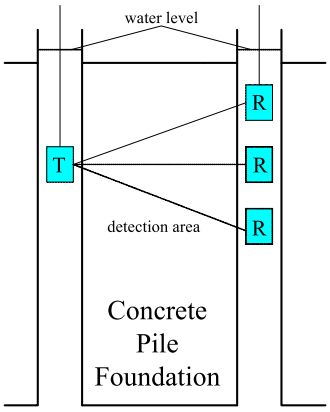

FIGURE 10. Sector scanning process.

FIGURE 11. Field test photo.

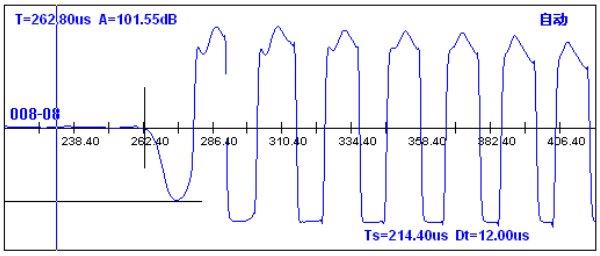

FIGURE 12. Measurement waveform collected by receiving sensor.

transmitting sensor was moved upward to the second test point. We sampled all the test point data at the receiving end by the same method until the transmitting sensor reached the top test point (the 14th test point) and data acquisition was completed.

During the sampling process, one test point was sampled at a time. Fig. 12 is the waveform recorded by the receiving sensor at the 8th receiving position after the transmitting sensor was excited at the 8th transmitting position. The time difference of recording the first wave is the time of sound travel at the test point. In the actual test, 14 sectors were tested, with 14 test points for each sector, yielding 196 data points on the time of sound travel. T1-T14 represent the 14 transmitting positions of the transmitting sensor respectively, while R1-R14 represent the 14 different receiving positions for each transmitting position, respectively. The waveforms of all test points were recorded according to the process shown in Fig.10, and the time of sound travel in each test point is listed in Table 4. Therefore, the data in the table show the time of sound travel when the ultrasound propagates from the transmitting position to the corresponding receiving position. For example, for T3 and R5, the data in the corresponding

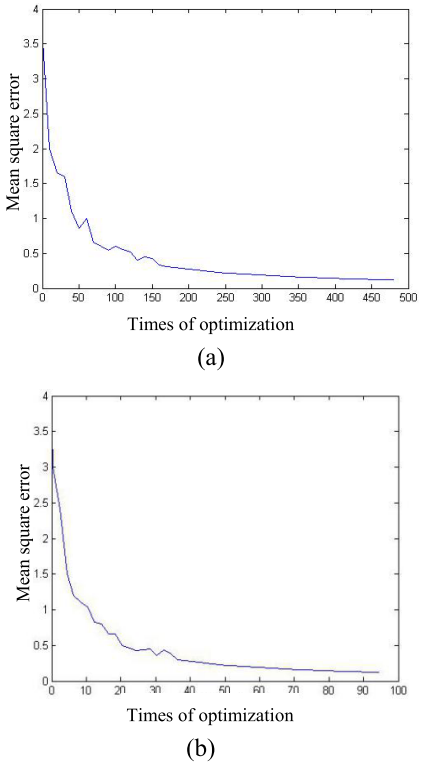

FIGURE 13. Mean-square deviation curves of the two algorithms. (a) Single GA; (b)SAGA.

grid show that the time of ultrasonic wave travel is 0.2768 ms from the T3 position to the R5 position.

C. PROCESSING AND ANALYSIS OF EXPERIMENTAL DATA

The GA and SAGA algorithms are used for the tomographic inversion processing of the experimental test data, and the imaging results were analyzed and compared.

The imaging convergence curves of the two algorithms for the imaging process are shown in Fig. 13. It can be seen from the figures that the mean square deviation of travel time of the two inversion algorithms decreases gradually with the increase of iteration times, and the travel time fitting degree of the two algorithms are both very high. The fitting deviation with the GA is 0.625% and 0.596% with SAGA. In terms of computing speed, there is a certain number of populations in each generation of GA, which results in a large number of calculations for each generation, and more iterations and slower computing speed. In SAGA, because of the addition of the simulated annealing process, this process has an accelerating effect on the whole search process. This makes the algorithm easier to converge than GA, so the number of iterations is smaller and the calculation speed is higher.

The imaging results after GA and SAGA processing of the detected data are shown in Fig. 14. The area surrounded by the dashed line boxes are defect areas. The location and area of the defects is correctly reflected in both figures, but the high-speed defect area in the lower half of the figure is

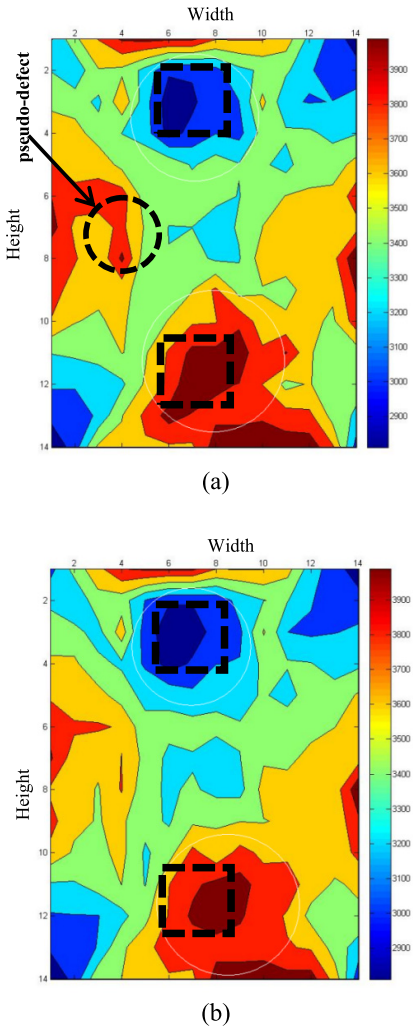

FIGURE 14. Processing inversion imaging result with the two algorithms. (a) SingleGA; (b) SAGA.

obviously larger than the actual defect area in Fig. 14(a), and there is a pseudo-defect area in the left of the figure center. The imaging result with SAGA in Fig. 14(b) is better, and the defect area is more consistent with the actual defect size. In the two figures, the position of the high-speed defect (C) is slightly deviated. It may be that when the high-speed mortar block is placed, some deviations occur in the mortar block due to the pouring, and the imaging result also deviates.

In addition, the calculated data of the two inversion algorithms are compared in Table 5. The measured average sound velocity of the specimen was 3515.8 m/s, and the background sound velocity of the GA inversion was 3748.2 m/s, with a relative error of 6.61%. The background sound velocity of SAGA inversion was 3587.8m /s, and the relative error was only 2.05%. From the relative difference of sound velocities between the low-velocity defect area and the high-velocity defect area and the background, the imaging results of SAGA inversion are more pronounced and the defect properties are easier to identify.

TABLE 5. Comparison of calculation data for the two inversion algorithms.

Inversion algorithm	Background velocity (m/s)	Inversion Background velocity (m/s)	Relative error (%)	Inversion defects velocity of (low / high speed defect) (m/s)	Relative difference between defects and background (low / high speed defect) (%)
GA	3515.8	3748.2	6.61	3409.8/3936.8	-9.03/5.03
SAGA		**3587.8**	**2.05**	**2912.0/4074.5**	**-18.84/13.57**

V. CONCLUSION

In this paper, a tomographic inversion image reconstruction technique based on SAGA is proposed based on practical requirements of quality testing for concrete pile foundation structures. By establishing the augmented objective function of quadratic optimization and combining the fast adaptive optimization search ability of GA with the control ability of SAA to global search, the global optimal solution is calculated quickly, and the reconstructed image of the detection area is obtained accurately through inversion. Numerical simulations have shown that the inversion imaging results calculated by the SAGA are more accurate and steady than the ones calculated by single GA under the same test conditions. The inversion results for an experimental test data of pile foundation specimen further show that compared with the single GA calculation process and imaging results, SAGA not only has fewer iterations and faster calculation speed, but also reflects the abnormal areas more accurately and clearly, thus facilitating the identification of the defects' properties. The results of this research have great application value in practical testing applications and structural safety assessment.

REFERENCES

[1] C. H. Pang, K. Y. Yong, Y. K. Chow, and J. Wang, "The response of pile foundations subjected to shield tunnelling," in *Proc. 5th Int. Conf. TC28 ISSMGE*. Leiden, The Netherlands: Business Press, 2006, pp. 737–743.

[2] H. Chen, D. Yuan, F. Wang, and M. Wang, "Study on shield cutting parameters when cutting big diameter piles," *China Civil Eng. J.*, vol. 49, no. 10, pp. 103–110, 2016.

[3] Z. Ji, S. Xueming, C. Xiaoling, and L. Ying, "Development of ultrasonic wave computer tomography technology and its application to nondestructive detection of concrete," *Chin. J. Eng. Geophys.*, vol. 5, no. 5, pp. 596–601, 2008.

[4] H. Chai, S. Momoki, Y. Kobayashi, D. G. Aggelis, and T. Shiotani, "Tomographic reconstruction for concrete using attenuation of ultrasound," *NDT & E Int.*, vol. 44, no. 2, pp. 206–215, 2011.

[5] Y. Jiang, F. Xu, B. Xu, E. S. Vargas, and A. Gallego, "Application of acoustic emission tomography in concrete structures," *J. Southeast Univ. (Natural Sci. Ed.)*, vol. 44, no. 4, pp. 822–826, 2014.

[6] Q.-H. Dong, "Newly developments of ultrasonic and acoustic wave testing of concrete," *Concrete*, vol. 17, no. 11, pp. 33–36, 2005.

[7] Q. Li, L. Shi, and D. Liang, "Research on 2D imaging technique for concrete cross section," *Chin. J. Acoust.*, vol. 29, no. 1, pp. 85–96, 2010.

[8] Q. Li, L. Shi, G. Wu, and D. Liang, "Research on improving quality of imaging of concrete structure," *Chin. J. Sci. Instrum.*, vol. 28, no. 4, pp. 2441–2445, 2008.

[9] B. Jiang, W. Zhao, and W. Wang, "Improved ultrasonic computerized tomography method for STS (Steel Tube Slab) structure based on compressive sampling algorithm," *Appl. Sci.*, vol. 7, no. 5, p. 432, 2017.

[10] B. Jiang, P. Jia, W. Zhao, and W. Wang, "The application of compressive sampling in rapid ultrasonic computerized tomography (UCT) technique of steel tube slab (STS)," *PLoS ONE*, vol. 13, no. 1, 2018, Art. no. e0190281.

[11] V. K. Karastathis, P. N. Karmis, G. Drakatos, and G. Stavrakakis, "Assessment of the dynamic properties of highly saturated concrete using one-sided acoustic tomography. Application in the Marathon Dam," *Construct. Building Mater.*, vol. 16, pp. 261–269, Jul. 2002.

[12] J. Cheng, L. Lia, and S. Yua, "Assessing changes in the mechanical condition of rock masses using P-wave computerized tomography," *Int. J. Rock Mech. Mining Sci.*, vol. 43, no. 4, pp. 503–678, 2006.

[13] Q. Li, H. Ma, and W. Chen, "Application of improved computerized tomography algorithm in concrete ultrasonic imaging," *Failure Anal. Provention*, vol. 7, no. 2, pp. 104–108, 2012.

[14] H. Lu, Y. Li, T. Uemura, Z. Ge, X. Xu, L. He, S. Serikawa, and H. Kim, "FDCNet: Filtering deep convolutional network for marine organism classification," *Multimedia Tools Appl.*, vol. 77, no. 17, pp. 21847–21860, 2017.

[15] X. Xu, H. Lu, J. Song,Y. Yang, H. T. Shen, and X. Li, "Ternary adversarial networks with self-supervision for zero-shot cross-modal retrieval," *IEEE Trans. Cybern.*, to be published. doi: 10.1109/TCYB.2019.2928180.

[16] Z. Wang and G. Liu, "An experimental study on acoustic travel time tomography of concrete component," *China Civil Eng. J.*, vol. 38, no. 6, pp. 110–114, 2005.

[17] Q. Li, Y. Wang, and R. Liu, "Research on ultrasonic computerized tomography imaging method of concrete materials based on simulated annealing genetic algorithm," *Trans. Nanjing Univ. Aeronaut. Astronaut.*, vol. 32, no. 3, pp. 341–347, 2015.

[18] G. Victor, *Structural Health Monitoring with Piezoelectric Wafer Active Sensors: With Piezoelectric Wafer Active Sensors*. Amsterdam, The Netherlands: Elsevier, 2014, pp. 357–394. doi: 10.1016/C2013-0-00155-7.

[19] L. Yu and G. Victor, "*In situ* 2-D piezoelectric wafer active sensors arrays for guided wave damage detection," *Ultrasonics*, vol. 48, no. 2, pp. 117–134, 2008.

[20] W. Hao-Quan, "Improvement and realization of linear travel-time interpolation ray tracing algorithm," *Russian J. Nondestruct. Test.*, vol. 46, no. 9, pp. 690–697, 2010.

[21] W. Xiong, Z. Zhou, and K. Yu, "Concrete ultrasonic tomography imaging and improvement based on curved path," *Rock Soil Mech.*, vol. 32, no. 2, pp. 629–634, 2011.

[22] X. Xu, L. He, A. Shimada, R.-I. Taniguchi, and H. Lu, "Learning unified binary codes for cross-modal retrieval via latent semantic hashing," *Neurocomputing*, vol. 213, pp. 191–203, Nov. 2016.

[23] G. Liu, Z. Wang, and J. Sun, "Elastic Wave tomography and its application to civil engineering," *China Civil Eng. J.*, vol. 36, no. 5, pp. 76–82, 2003.

[24] A. H. Andersen and A. C. Kak, "Simultaneous algebraic reconstruction technique (SART): A superior implementation of the art algorithm," *Ultrason. Imag.*, vol. 6, no. 1, pp. 81–94, 1984.

[25] X. Xu, F. Shen, Y. Yang, H. T. Shen, and X. Li, "Learning discriminative binary codes for large-scale cross-modal retrieval," *IEEE Trans. Image Process.*, vol. 26, no. 5, pp. 2494–2507, May 2017.

[26] Y. Sun, Q. Li, and L. Huang, "Application of simulated annealing genetic algorithm for concrete structures CT imaging," *Piezoelectrics Aciystooptics*, vol. 35, no. 4, pp. 487–490 and 495, 2013.

[27] J. Martina, K. J. Broughton, A. Giannopolous, M. S. A. Hardy, and M. C. Forde, "Ultrasonic tomography of grouted duct post-tensioned reinforced concrete bridge beams," *NDT & E Int.*, vol. 34, no. 2, pp. 107–113, 2001.

[28] W. Jiang and J. Zhang, "First-arrival traveltime tomography with modified total-variation regularization," *Geophys. Prospecting*, vol. 65, no. 5, pp. 1138–1154, 2017.
[29] Z. Huang, X. Ji, and L. Huang, "Ultrasonic computerized tomography for structural concrete based on chaotic simulated annealing and re-annealing algorithm," *J. Railway Sci. Eng.*, vol. 5, no. 1, pp. 1–5, 2008.
[30] C. Rose, "Low mean internodal distance network topologies and simulated annealing," *IEEE Trans. Commun.*, vol. 40, no. 8, pp. 1319–1326, Aug. 1992.
[31] D. Du, E. He, and L. Li, "A dynamics model updating method of nozzle based on improved simulation annealing algorithm," *J. Astronaut.*, vol. 39, no. 6, pp. 632–638, 2018.
[32] H. Lu, Y. Li, T. Uemura, H. Kim, and S. Serikawa, "Low illumination underwater light field images reconstruction using deep convolutional neural networks," *Future Gener. Comput. Syst.*, vol. 82, pp. 142–148, May 2018.
[33] X. Xu, L. He, H. Lu, L. Gao, and Y. Ji, "Deep adversarial metric learning for cross-modal retrieval," *World Wide Web*, vol. 22, no. 2, pp. 657–672, 2019.
[34] L. Qin, J. Wang, H. Li, Y. Sun, and S. Li, "An approach to improve the performance of simulated annealing algorithm utilizing the variable universe adaptive fuzzy logic system," *IEEE Access*, vol. 5, pp. 18155–18165, 2017.
[35] C. He, Z. Wang, and X. Liu, "Magnetic property parameter identification of steel pole based on GA-PSO hybrid algorithm," *Chin. J. Sci. Instrum.*, vol. 38, no. 4, pp. 838–843, 2017.
[36] Y. Lin, H. Zhao, and H. Ding, "Solution of inverse kinematics for general robot manipulators based on multiple population genetic algorithm," *J. Mech. Eng.*, vol. 53, no. 3, pp. 1–8, 2017.
[37] Y.-H. Chou, S.-Y. Kuo, and Y.-T. Lo, "Portfolio optimization based on funds standardization and genetic algorithm," *IEEE Access*, vol. 5, pp. 21885–21900, 2017.
[38] W. Zhang, K. Yang, and M. Zhang, "An improved genetic simulated annealing algorithm to solve the unequal circle packing problem," *J. Northwestern Polytech. Univ.*, vol. 35, no. 6, pp. 1033–1039, 2017.
[39] W. Han, X. Jin, and H. Ren, "Defect reconstruction from MFL signals using genetic-simulated-annealing algorithm," *J. Basic Sci. Eng.*, vol. 15, no. 2, pp. 257–262, 2007.
[40] W. Wang, H. Zhang, J. P. Lynch, C. E. S. Cesnik, and H. Li, "Experimental and numerical validation of guided wave phased arrays integrated within standard data acquisition systems for structural health monitoring," *Struct. Control Health Monitor.*, vol. 25, no. 6, p. e2171, 2018.
[41] W. Wang, H. Zhang, J. P. Lynch, C. E. S. Cesnik, and H. Li, "Numerical and experimental simulation of linear shear piezoelectric phased arrays for structural health monitoring," *Proc. SPIE*, vol. 10169, Apr. 2017, Art. no. 1016912. doi: 10.1117/12.2262945.

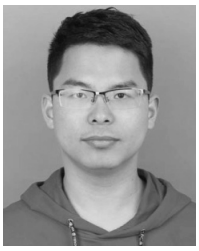

GUAN WANG was born in Shanxi, China, in 1996. He received the B.Sc. degree from Nanchang Hangkong University, in 2018, where he is currently pursuing the M.E. degree. His research interests include imaging algorithm and image processing.

YAO CHEN received the B.Sc. and M.Sc. degrees from the Liaoning University of Technology, in 2008 and 2011, respectively, and the Ph.D. degree from the Dalian University of Technology, in 2016. He is currently a Lecturer with Nanchang Hangkong University. His research interests include acoustic imaging test and signal processing for the anisotropic and heterogeneous materials.

QIUFENG LI was born in Jiangxi, China, in 1976. He received the B.Sc. and M.Sc. degrees from Nanchang Hangkong University, in 1998 and 2005, respectively, and the Ph.D. degree from the Nanjing University of Aeronautics and Astronautics, in 2008. He is currently a Professor with Nanchang Hangkong University. His research interests include acoustic imaging test, signal processing, and high resolution imaging algorithm.

CHAO LU was born in Jiangxi, China, in 1971. He received the B.Sc. degree in physics from Jiangxi Normal University, in 1995, the M.Sc. degree in physics from the University of Science and Technology of China, in 1998, and the Ph.D. from the China Academy of Railway Sciences, in 2009. He is currently a Professor with Nanchang Hangkong University. His research interests include acoustic non-destructive testing and high resolution imaging method.

GUO CHEN received the B.Sc. and M.Sc. degrees from Nanchang Hangkong University, in 2009 and 2012, respectively, where she is currently a Lecturer. Her research interests include acoustic non-destructive testing and signal processing for the anisotropic and heterogeneous materials.

LIXIA HUANG received the B.Sc. degree from the Henan University of Science and Technology, in 2007, and the M.Sc. degree from Zhejiang University, in 2017. She is currently a Lecturer with Nanchang Hangkong University. Her research interests include information management and imaging algorithm.